Anion-exchange synthesis of Ag_2S/Ag_3PO_4 core/shell composites with enhanced visible and NIR light photocatalytic performance and the photocatalytic mechanisms

Jun Tian[a], Tingjiang Yan[a,b,*], Zheng Qiao[a], Linlin Wang[a], Wenjuan Li[a], Jinmao You[a], Baibiao Huang[b,*]

[a] The Key Laboratory of Life-Organic Analysis, College of Chemistry and Chemical Engineering, Qufu Normal University, Qufu 273165, Shandong, PR China
[b] State Key Laboratory of Crystal Materials, Shandong University, Jinan 250100, Shandong, PR China

ARTICLE INFO

ABSTRACT

A series of Ag_2S/Ag_3PO_4 composites with well-defined core/shell structures were synthesized via an *in-situ* anion-exchange reaction between Ag_3PO_4 dodecahedrons and Na_2S solutions. The obtained samples were characterized by XRD, BET, AFS, SEM, TEM, EDX, XPS, DRS and PL. The Ag_2S/Ag_3PO_4 composites exhibited excellent photocatalytic activity towards the degradation of MO under both visible and NIR light irradiation. The optimal composite Ag_2S-5%/Ag_3PO_4 exhibited the highest visible-light-driven activity, which could degrade almost all MO within 120 min. Under NIR light irradiation, the Ag_2S-50%/Ag_3PO_4 composite showed the best photocatalytic activity and decomposed more than 30% of MO after 240 min of irradiation. Recycling experiments confirmed that the Ag_2S/Ag_3PO_4 composites had superior cycle performance and stability. The photocatalytic activity was highly dependent on the Ag_2S content and the well-defined core/shell structure. The enhancement in photocatalytic activity of Ag_2S/Ag_3PO_4 composites could be mainly ascribed to the efficient separation of photogenerated charge carriers between the intimate interface of Ag_2S shell and Ag_3PO_4 core. The *in-situ* formed Ag nanoparticles at surfaces of Ag_3PO_4 and Ag_2S during photocatalytic process acted as charge transmission bridges and electron trapping centers, respectively, resulting in the stable $Ag_2S/Ag/Ag_3PO_4$ Z-scheme system and $Ag/Ag_2S/Ag_3PO_4$ ternary system. Based on the experimental results, the possible photocatalytic mechanisms for MO degradation over Ag_2S/Ag_3PO_4 composites under both visible and NIR light irradiation were proposed.

1. Introduction

Since Fujishima and Honda discovered photocatalytic water-spitting on TiO_2 electrodes for hydrogen production in 1972 [1], research interest in semiconductor photocatalysis has grown significantly owing to its potential applications in environmental purification and solar energy conversion. Yet, the traditional photocatalytic materials, such as TiO_2 and ZnO, require UV light to be activated because of their large bandgap of ∼3.2 eV. It is generally known that UV light in the overall solar spectrum takes up only ∼5%, whereas the percentages of visible light and near-infrared (NIR) light are about ∼49% and ∼46%, respectively [2]. For better

use of solar energy, much effort has been devoted to extending the absorption of UV-active photocatalyst into visible light or NIR light region by adjusting the bandgap through noble metal deposition, metal/nonmetal dopant, coupling with upconversion material and so on [3–6]. On the other hand, some researchers have also paid considerable attention on the exploration of novel photocatalytic materials that are sensitive to visible light or NIR light, such as $In_{1-x}Ni_xTaO_4$ [7], $ZnIn_2S_4$ [8], g-C_3N_4 [9], Ag/AgX (X = Cl, Br, I) [10], $Cu_2(OH)PO_4$ [11], and so on.

Among the reported novel photocatalysts, silver orthophosphate (Ag_3PO_4) with a suitable band gap (2.36 eV) has received more attention in the fields of O_2 evolution from water and organic pollutant treatment under visible light irradiation [12]. However, some limitations inherent in the Ag_3PO_4 photocatalytic system should be paid more attention, such as the high solubility, the photo-corrosion issue and the fast recombination of photogenerated charge carriers (electrons and holes). Many strategies against its drawbacks have been reported. For example, Bi, Ye et al. inves-

tigated the facet effect on the photocatalytic properties of Ag_3PO_4 and synthesized single-crystalline Ag_3PO_4 rhombic dodecahedrons with only active {1 1 0} facets exposed [13]. They further fabricated Ag/Ag_3PO_4 heterostructures to improve the photocatalytic activity of Ag_3PO_4 [14,15]. Constructing heterostructure/composite photocatalysts has proven to be effective in reducing the recombination of charge carriers and strengthening the structural stability of singe component [16–19]. Many Ag_3PO_4-based composites including Ag_3PO_4/TiO_2 [20], $Ag_3PO_4/In(OH)_3$ [21], $Ag_3PO_4/BiVO_4$ [22], $Ag_3PO_4/BiOI$ [23], Ag_3PO_4/SnO_2 [24], Ag_3PO_4/g-C_3N_4 [25], $Ag_3PO_4/graphene$ oxide [26], Ag_3PO_4/SiO_2 [27], and so on have been fabricated and shown to be highly efficient in photocatalysis. More specially, the well interfacial connection in composite photocatalysts is considered to be crucial in promoting the photogenerated charge carries transfer and/or separation and thus the photocatalytic performance [28]. A solution to achieve strong interfacial contact is the preparation of composite photocatalysts with a core/shell structure [29]. For instance, Yu et al. fabricated core/shell structured PAN/Ag_3PO_4 nanofibers by combining electrospinning technology with ion exchange reaction and found that the introduction of PAN significantly enhanced visible light photocatalytic activity [30]. Highly efficient AgX/Ag_3PO_4 (X = Cl, Br, I) core–shell heterostructures have further been obtained by Bi et al. through the epitaxial growth method [31]. The coating of AgX shell promoted the effective separation of charge carries and simultaneously prevented the dissolution of the Ag_3PO_4 core–crystals, accounting for excellent catalytic activity and structural stability. The $Ag_3PO_4@g$-C_3N_4 core–shell composites synthesized by ultrasonication-chemisorption method were also shown to be efficient and stable in organic dye degradation under visible light irradiation [32]. Therefore, the design of core/shell structures between Ag_3PO_4 and an appropriate photocatalyst is an effective approach to improve the photocatalytic performance (both activity and stability) of Ag_3PO_4.

Ag_2S with a narrow band gap of around 1 eV and a large absorption coefficient in the entire solar spectrum, has received great attention as promising photocatalysts or photosensitizer for photo- or photoelectrocatalysts under visible and NIR light irradiation [33–35]. For example, Jiang et al. explored the wide application of Ag_2S as photocatalyst worked under visible and NIR light irradiation [36]. Li et al. developed the Ag_2S–Ag–TiO_2 hybrid structures and found that the ternary hybrid exhibited dramatically enhanced performance in photocatalytic hydrogen production under full-spectrum irradiation [37]. More recently, Ag_2S/Ag_3PO_4 composites with outstanding visible-light-driven photocatalytic performance have also been fabricated in view of the suitable band structure between Ag_2S and Ag_3PO_4. Tang et al. synthesized $Ag@(Ag_2S/Ag_3PO_4)$ composites via an anion-exchange method and a subsequent calcination treatment [38]. Nevertheless, the high-temperature treatment led to particle agglomeration/coarsening and moreover adverse effects on charge transfer at the ternary interface. To improve the interfacial effect, Ma et al. developed an in situ synthesis strategy to achieve Ag_3PO_4/Ag_2S composites by assembling of Ag_3PO_4 nanoparticles on two-dimensional Ag_2S sheets [39]. However, the exposed Ag_3PO_4 nanoparticles in Ag_3PO_4/Ag_2S composites still suffered from the structural instability issue in aqueous solution. In consideration of the above discussion, constructing of Ag_2S/Ag_3PO_4 core–shell composites may be a feasible strategy to resolve all issues. The cover of Ag_2S nanoparticles shell on Ag_3PO_4 core can not only promote the effective separation of charge carries but also improve the structural stability of the composites. Besides, due to the light sensitization effect of Ag_2S shell, the Ag_2S/Ag_3PO_4 may possess photocatalytic performance under NIR light illumination. To our knowledge, there are no reports concerning the NIR-light-driven photocatalytic performance of Ag_2S/Ag_3PO_4 composites. Further-

more, the structure–property relationship and the corresponding photocatalytic mechanisms still remain the challenge.

Herein, we firstly report the synthesis of Ag_2S/Ag_3PO_4 composites with well-defined core/shell structure according to the anion-exchange principle. The highly dispersed Ag_2S nanoparticles can in-situ grow onto the surfaces of Ag_3PO_4 dodecahedrons. During the degradation of methyl orange (MO) under visible light and NIR light irradiation, the Ag_2S/Ag_3PO_4 composites exhibit much higher photocatalytic activities than pure Ag_2S and Ag_3PO_4. The activity of the composites is found to be highly dependent on the Ag_2S content and the core/shell structure. Ag_2S/Ag_3PO_4 composites also display excellent stability irradiated under visible and NIR light. The possible photocatalytic mechanisms under both conditions are thereby proposed.

2. Experimental section

2.1. Materials

All reagents were of analytical grade and used without further purification. Silver nitrate ($AgNO_3$), hexamethylenetetramine (HMT), sodium dihydrogen phosphate (NaH_2PO_4), sodium sulphide (Na_2S), terepthalic acid (TA), ammonium oxalate (AO), benzoquinone (BQ) and tertbutyl alcohol (TBA) were purchased from Sigma–Aldrich India. Double distilled water was used throughout the study.

2.2. Sample preparation

2.2.1. Synthesis of Ag_3PO_4 dodecahedrons

Ag_3PO_4 dodecahedrons were prepared by a simple precipitation method. In a typical synthesis, 1.87 mmol $AgNO_3$ was dissolved in 40 mL distilled water. Then 0.315 g HMT was added to the above suspension under intensive stirring and the entire solution became a milky white color. After stirring 15 min, NaH_2PO_4 aqueous solution (0.15 M) was added with drop by drop to the above solution, and golden yellow precipitation would be formed. The as-obtained precipitate was washed and kept in an oven at 60 °C.

2.2.2. Synthesis of Ag_2S/Ag_3PO_4 composites

Ag_2S/Ag_3PO_4 composites were obtained through an in-situ anion exchange method in dark conditions at room temperature. The obtained Ag_3PO_4 (1.0 g) powder was dispersed in 50 mL of distilled water and suspension was ultrasonicated for 0.5 h. Subsequently certain amounts of Na_2S solutions (1–80 mL, 0.01 M) were added drop wise into the above Ag_3PO_4 suspension with constant stirring. The obtained suspension was vigorously stirred for 4 h. The precipitates were collected, washed with deionized water several times and finally dried at 60 °C for 24 h. The series of Ag_2S/Ag_3PO_4 composites were obtained by varying the concentration of Na_2S aqueous solution and denoted Ag_2S-X%, where X% is the molar ratio of S relative to P. The pure Ag_2S samples were obtained by a simple precipitation reaction between Na_2S solutions and $AgNO_3$ solutions at room temperature.

2.3. Sample characterizations

X-ray diffraction patterns (XRD) were collected on a Rigaku MinFlex II equipped with Cu $K\alpha$ irradiation. BET surface area was performed on a Micromeritics ASAP 2000 analyzer. Morphologies and composition of the samples were observed by field emission scanning electron microscope (FE-SEM) (Hitachi S-4800), transmission electron microscope (TEM) (JEM-2010) and energy dispersive X-ray spectroscopy (EDX). The content of S and P was quantified on atomic fluorescence spectroscopy (AFS, AFS-9600). X-ray photoelectron spectra (XPS) were recorded on an ESCALAB
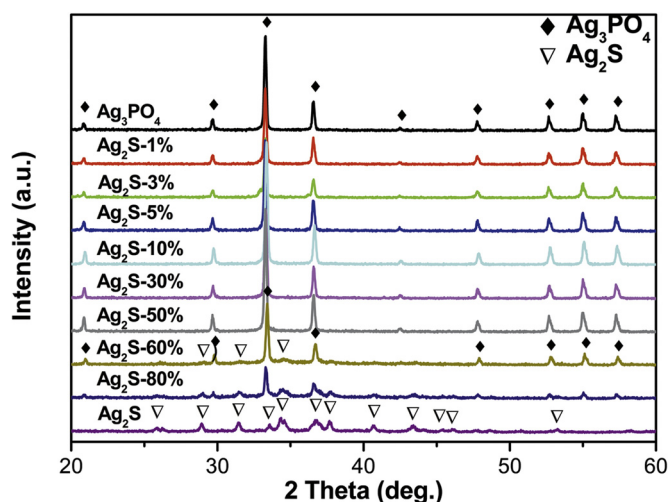
Fig. 1. XRD patterns of pure Ag_3PO_4, Ag_2S and Ag_2S/Ag_3PO_4 composites.

Table 1
The specific surface areas of the as-prepared samples.

Samples	Specific surface area (m^2/g)	The molar ratio of S/P (%)
Ag_3PO_4	0.8	0
Ag_2S-3%	1.1	2.56
Ag_2S-5%	2.4	4.02
Ag_2S-30%	4.5	23.74
Ag_2S-50%	4.8	38.24
Ag_2S-80%	4.7	59.36
Ag_2S	7.2	–

250 photoelectron spectroscope (Thermo Fisher Scientific) with monochromatic Al $K\alpha$ radiation ($E = 1486.2$ eV). UV–vis–NIR diffuse reflectance spectra (DRS) were collected using a Varian Cary 500 Scan system equipped with an integrating sphere attachment. Steady-state photoluminescence (PL) spectra of the samples were performed on an Edinburgh Analytical Instruments F-4600 coupled with a time correlated single-photo counting system. Transient PL spectra were performed on an Edinburgh Analytical Instruments FLSP-920 using a 375 wavelength pulse laser (pulse width 70 ps). Electrochemical impedance (EIS) was recorded on a CHI-660B electrochemical workstation (Chenhua Co.) in a standard three-electrode configuration.

2.4. Evaluation of photocatalytic activity

Photocatalytic experiments were performed in an aqueous solution at ambient temperature irradiated by visible light (300 W Xe arc lamp) and NIR light (300 W infrared lamp), which was respectively obtained by using cutoff filters to remove light of $\lambda < 400$ nm or $\lambda < 760$ nm. Briefly, 35 mg of photocatalyst was suspended in 80 mL aqueous solution of MO dye (10 ppm). Prior to irradiation, the suspension was magnetically stirred in dark for 0.5 h to establish an adsorption–desorption equilibrium. A 4 mL aliquot was taken at several minutes intervals during the experiment and centrifuged to remove the powders. The residual concentration of dye was analyzed on a Shanghai Youke UV756CRT spectrophotometer. The degradation percentage is reported as C/C_0, where C_0 is the initial concentration of dye, and C represents the corresponding concentration at a certain time interval. The stability was tested as follows: after each MO degradation reaction, the suspension was filtered and the solids were washed with water and dried at 60 °C in air. Then the regenerated product was employed to degrade a new 10 ppm MO aqueous solution for another test under the same visible light irradiation. During the radical-trapping experiments, 35 mg catalyst with TBA (1 mL) or AO (11.7 mg) or BQ (1.2 mg) was dispersed in MO aqueous solution (80 mL, 10 ppm) before visible light irradiation.

3. Results and discussion

3.1. Texture properties

The phase composition and crystal properties of the obtained samples are analyzed by XRD. Fig. 1 shows the XRD patterns of the Ag_3PO_4, Ag_2S and Ag_2S/Ag_3PO_4 composites. It can be observed that the diffraction peaks of Ag_3PO_4 are indexed to the cubic phase of

Ag_3PO_4 crystal (JCPDS No. 06-0505) and no other diffraction peaks are detected, which indicates that the produced Ag_3PO_4 has high purity without other impurities. Compared with Ag_3PO_4, Ag_2S displays relatively weak and broad diffraction peaks. These peaks are attributed to the monoclinic structure (JCPDS No.14-0072). The broad diffraction peaks of Ag_2S are attributed to the relatively small crystalline size [36,40]. As for the Ag_2S/Ag_3PO_4 composites, no obvious diffraction peaks of Ag_2S are observed in Ag_2S/Ag_3PO_4 when the amount of Ag_2S is lower than 50%. This may be due to the fact that Ag_2S nanoparticles are highly dispersed on the surface of Ag_3PO_4 dodecahedrons. However, with the increase of the loading amount of Ag_2S above 60%, the intensity of diffraction peaks of Ag_2S increases whereas that of Ag_3PO_4 decreases simultaneously. It is notable that no characteristic peaks attributed to metal silver and other new compounds are detected in all Ag_2S/Ag_3PO_4 samples, indicating that Ag_2S and Ag_3PO_4 maintain as pure phase and no impurities formed in Ag_2S/Ag_3PO_4 composites.

The BET surface area of the pure samples (Ag_3PO_4 and Ag_2S) and Ag_2S/Ag_3PO_4 composites has been measured. From Table 1, we can see that pure Ag_3PO_4 exhibits small specific surface area of 0.8 m^2/g while pure Ag_2S have a slightly large value of 7.2 m^2/g. The growth of Ag_2S onto Ag_3PO_4 has little influence on the BET surface area of the composites, which indicates the negligible effect of surface area on the followed photocatalytic activity. The actual molar ratio of S/P in the Ag_2S/Ag_3PO_4 composites is determined by AFS and the results are shown in Table 1.

3.2. Microstructures

The SEM images of Ag_3PO_4, Ag_2S as well as Ag_2S/Ag_3PO_4 composites are presented in Fig. 2. Fig. 2a shows that Ag_3PO_4 samples appear with the homogeneous dodecahedral morphology with an average diameter of 2 μm. It can be clearly observed that the Ag_3PO_4 particles have clean and smooth surfaces. As compared, pure Ag_2S particles are irregular aggregates which are composed of crystal grains with diameters of 30–80 nm (Fig. 2b, Fig. S1), consistent with the reported result [36]. In the case of Ag_2S/Ag_3PO_4 composites, novel core/shell heterocrystals consisting of Ag_3PO_4 dodecahedrons core and Ag_2S nanoparticles shell are obtained by the anion-exchange process (Fig. S2), similar to the AgX (X = Cl, Br, I)/Ag_3PO_4 heterocrystals reported by Bi et al. [31]. It should be noted that the core/shell structure and the size of Ag_2S nanoparticles are highly dependent on the amount of S^{2-}. When a low amount (1–5%) of Na_2S is introduced, tiny and uniform Ag_2S nanoparticles are highly dispersed on the surface of Ag_3PO_4 dodecahedrons (Fig. 2c–e). With increasing the Na_2S amount (10–50%), more and large Ag_2S nanoparticles are covered on the Ag_3PO_4 surfaces (Fig. 2f–h). Further increasing the Na_2S amount (60–80%) obviously destroys the well-defined core/shell structure. Instead, only broken Ag_3PO_4 particles and detached Ag_2S aggregates can be found in these composites (Fig. 2i and Fig. S3).

The microstructure and composition of the Ag_2S/Ag_3PO_4 composites are further investigated by TEM and EDX. The TEM images for the Ag_2S-5%/Ag_3PO_4 sample show that a few of Ag_2S nanopar-
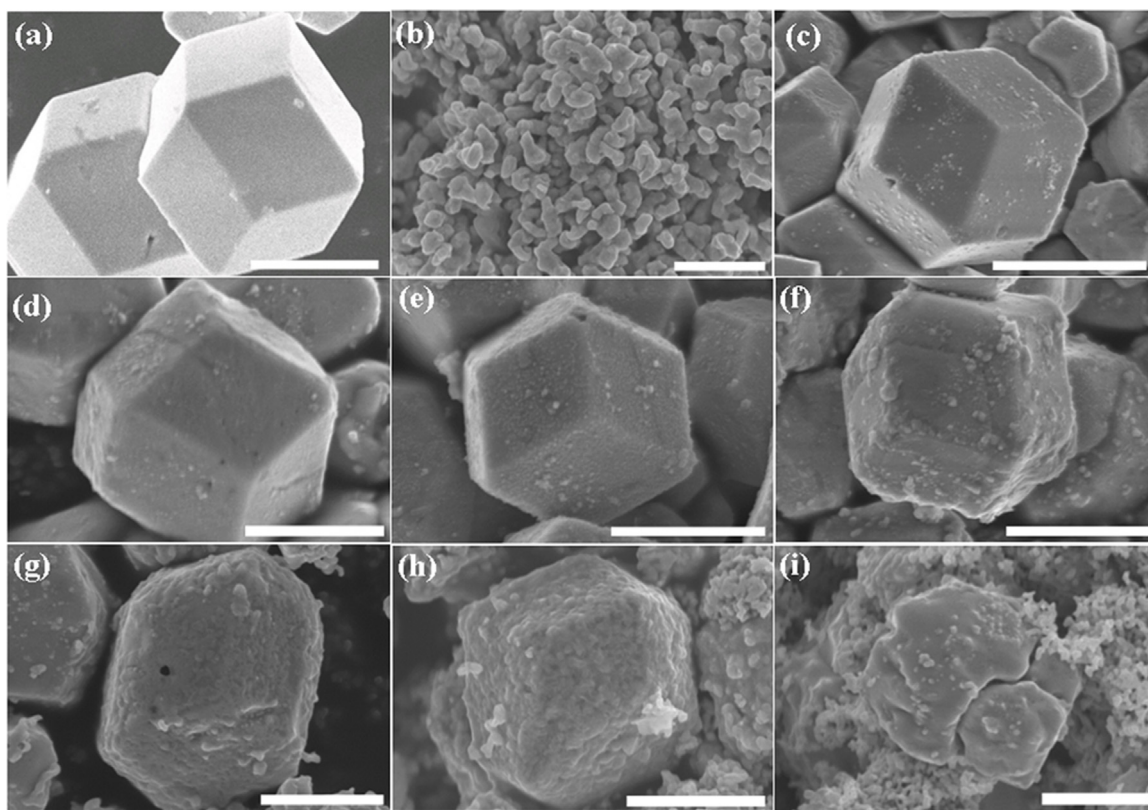
Fig. 2. SEM images of (a) pure Ag$_3$PO$_4$, (b) pure Ag$_2$S, and Ag$_2$S/Ag$_3$PO$_4$ composites: (c) Ag$_2$S-1%, (d) Ag$_2$S-3%, (e) Ag$_2$S-5%, (f) Ag$_2$S-10%, (g) Ag$_2$S-30%, (h) Ag$_2$S-50%, (i) Ag$_2$S-60%, (all scale bars are 1 µm).

ticles with size below 5 nm are deposited on the surface of Ag$_3$PO$_4$ dodecahedrons (Fig. 3a and b and Fig. S4a and b). Due to the limited amount of S^{2-}, the Ag$_3$PO$_4$ surface is partially covered by Ag$_2$S nanoparticles, shown as the diagram insert in Fig. 3b. The EDX spectrum (Fig. 3c) indicates that the Ag$_2$S-5%/Ag$_3$PO$_4$ sample contains Ag, P, S and O elements, confirming the presence of Ag$_2$S and Ag$_3$PO$_4$. For Ag$_2$S-50%/Ag$_3$PO$_4$ sample, it can be observed that Ag$_2$S nanoparticles with increasing amounts and large sizes ranging from approximately 20 to 50 nm are uniformly distributed on the Ag$_3$PO$_4$ dodecahedrons (Fig. 3d and e and Fig. S4c and d), resulting in the fully covered core/shell structures (shown as the diagram in Fig. 3e). The EDX spectrum (Fig. 3f) also proves the coexistence of Ag$_3$PO$_4$ and Ag$_2$S. Accordingly, the well-defined Ag$_2$S/Ag$_3$PO$_4$ core/shell composites can be fabricated by the anion-exchange route. That is, S^{2-} ions substitute for the [PO$_4$]$^{3-}$ units on the surface of Ag$_3$PO$_4$ dodecahedrons to form Ag$_2$S nanoparticles, because the much smaller K_{sp} value (6.6×10^{-50}) of Ag$_2$S than Ag$_3$PO$_4$ (1.4×10^{-16}) easily facilitates this conversion [41]. The nucleation and growth of Ag$_2$S nanoparticles is highly dependent on the concentration of S^{2-} during this ion-exchange process.

XPS analyses are carried out on the typical Ag$_2$S-5%/Ag$_3$PO$_4$ and Ag$_2$S-50%/Ag$_3$PO$_4$ composites to evaluate the chemical valence state of the elements, and the results are shown in Fig. 4. The full-scale XPS pattern is shown in Fig. 4a, which indicates the existence of Ag, O, P and S elements in both samples. The high resolution XPS spectra of Ag 3d show that there are two peaks located at 367.8 and 373.8 eV (Fig. 4b), which can be respectively attributed to Ag 3d$_{5/2}$ and Ag 3d$_{3/2}$ binding energies in Ag$_3$PO$_4$ or Ag$_2$S [13,40,42]. Peak fitting of Ag 3d spectra indicates the coexistence of metallic Ag^0 and Ag$^+$ in both composites. The relative percentages of metallic Ag^0 in Ag$_2$S-5%/Ag$_3$PO$_4$ and Ag$_2$S-50%/Ag$_3$PO$_4$ are estimated to be 7.5% and 23.3%, respectively, suggesting that more metallic Ag^0 are formed in the high concentration of S^{2-} system. In the O 1s spectra

(Fig. 4c), the main peak at 530.7 eV is assigned to the oxygen in the Ag$_3$PO$_4$ crystal lattice and the weak peak at 532.7 eV is due to the chemisorbed H$_2$O or OH$^-$ on the surface of the samples. The P 2p peak is located at 132.5 eV (Fig. 4d), affirming that the valence state of P is +5. In the case of the S 2p spectra, the two S 2p$_{3/2}$ and S 2p$_{1/2}$ peaks located at around 161.8 and 163.0 eV are characteristics of sulfur anions in the lattice of Ag$_2$S correspondingly [36,43,44]. It is apparent noted that the peak intensity of P 2p in Ag$_2$S-5%/Ag$_3$PO$_4$ is much stronger than that in Ag$_2$S-50%/Ag$_3$PO$_4$, while that of S 2p in Ag$_2$S-5%/Ag$_3$PO$_4$ is weaker than that in Ag$_2$S-50%/Ag$_3$PO$_4$. This result evidently suggests that more Ag$_2$S nanoparticles are deposited on the Ag$_3$PO$_4$ surface with increasing S^{2-} amount, quite consistent with the SEM and TEM results.

3.3. Optical properties

The optical properties of the samples are investigated and the corresponding DRS spectra are shown in Fig. 5a. Ag$_3$PO$_4$ dodecahedrons exhibit strong absorption in the UV and visible light region. A steep absorption edge is located at approximately 520 nm. Ag$_2$S nanoparticles exhibit a remarkable absorption in the entire UV–vis–NIR region. The absorption edge can be extended to around 1400 nm, indicating that it can significantly adsorb more light in the visible-NIR region as compared with pure Ag$_3$PO$_4$. Accordingly, for the Ag$_2$S/Ag$_3$PO$_4$ composites, one can see that the absorption edge demonstrates a gradual red-shift from 520 nm to 1500 nm with the increase of Ag$_2$S contents. The obvious red-shift of absorption edge for Ag$_2$S/Ag$_3$PO$_4$ samples is attributed to the excellent sensitization effect of Ag$_2$S, which can absorb more visible and NIR light and make the Ag$_2$S/Ag$_3$PO$_4$ composites effectively harness the full spectrum of solar light to strengthen the photocatalytic activities. Moreover, the majority of Ag$_2$S/Ag$_3$PO$_4$ composites are found to show much larger light absorption than Ag$_2$S. This might be
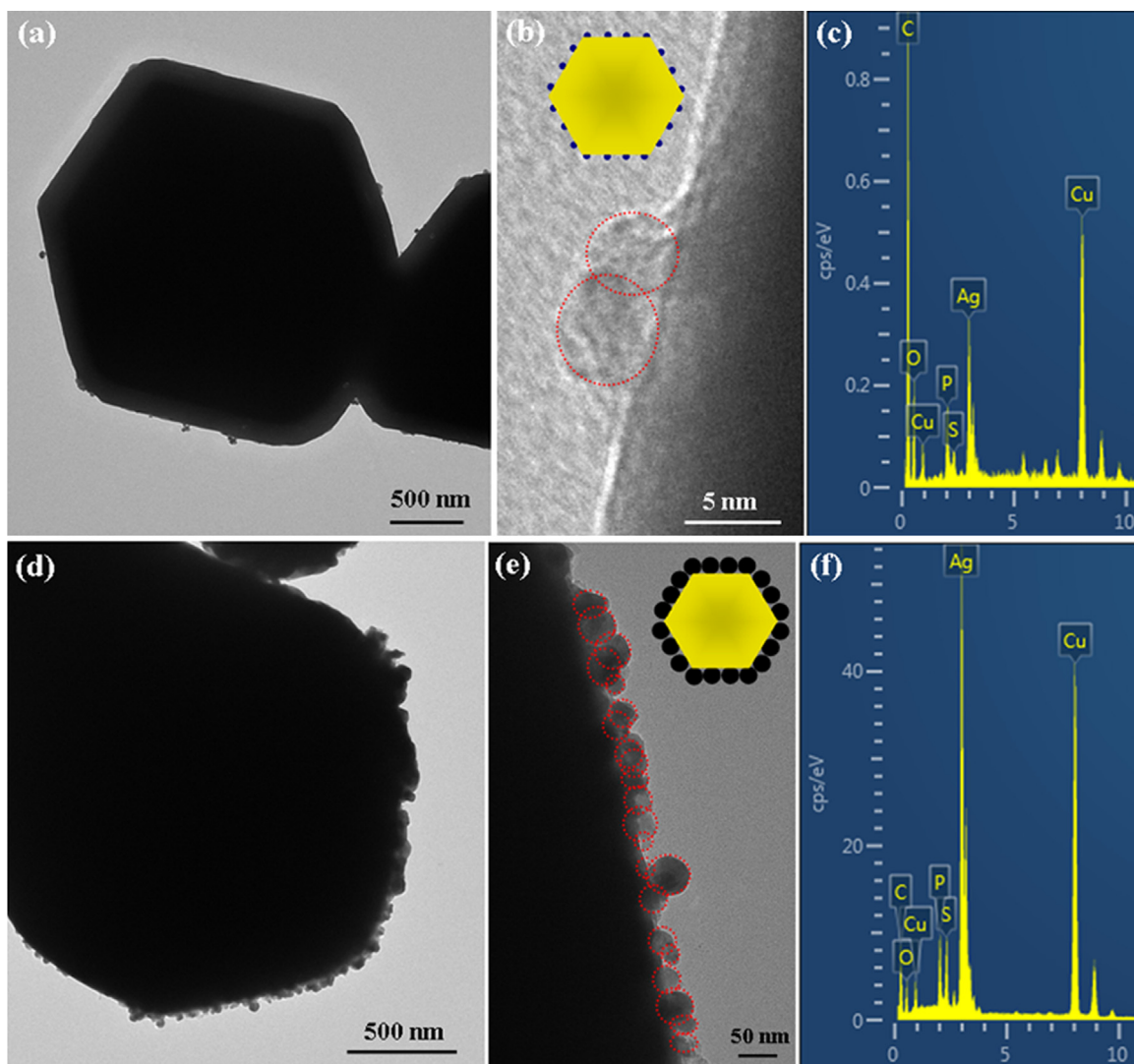
Fig. 3. TEM and EDX pattern of (a–c) Ag_2S-5%/Ag_3PO_4 and (d–f) Ag_2S-50%/Ag_3PO_4 composites.

attributed to the plasmon resonance of metallic Ag^0 *in-situ* formed during ion-exchange process [10,45].

The band gap energy (E_g) of Ag_2S and Ag_3PO_4 is calculated by the following equation: $\alpha h\nu = A(h\nu - E_g)^{n/2}$, where α, h, ν and A are the absorption coefficient, Planck constant, light frequency and proportionality, respectively; n is decided from the properties of the transition in a semiconductor. Ag_3PO_4 is an indirect band semiconductor, and the value of n is 4; Ag_2S is reported to be a direct band semiconductor [46], and the value of n is 1. As shown in Fig. 5b and c, the band gaps of Ag_3PO_4 and Ag_2S are about 2.33 and 0.99 eV, respectively, which are in accordance with the previous reports [12,42]. Moreover, it is known that the band edge positions of the conduction band (CB) and the valence band (VB) of photocatalysts also play a crucial role in determining their photocatalytic activity and can be achieved by the empirical formula: $E_{VB} = X - E_0 + 1/2E_g$ and $E_{CB} = X - E_0 - 1/2E_g$, in which X is the absolute electronegativity of the semiconductor, determined by the geometric mean of the absolute electronegativity of constituent atoms, which is defined as the arithmetic mean of the atomic electron affinity and the first ionization energy; E_0 is the energy of free electrons on the hydrogen scale (about 4.5 eV); and E_g is the band gap of the semiconductor. Accordingly, the E_{CB} and E_{VB} of Ag_3PO_4 are determined to be 0.25 and 2.67 eV, while those of Ag_2S are −0.025 and 0.965 eV. The appropriate energy level of the CB and VB edges assures that Ag_2S

can act as sensitizers, which makes Ag_3PO_4 highly active under visible light and NIR light.

3.4. Photocatalytic activity

As indicated above, the results from full solar spectrum absorption of the Ag_2S/Ag_3PO_4 composites predict their enhanced photocatalytic activity in wide spectral range of solar light. Herein, the photocatalytic activity of the Ag_2S/Ag_3PO_4 composites is investigated for the decomposition of MO under visible and NIR light irradiation, respectively.

3.4.1. Visible-light-driven photocatalytic property

As shown from Fig. 6a, pure Ag_3PO_4 and all Ag_2S/Ag_3PO_4 composites display negligible adsorption capability for MO due to the low surface area and negatively charged surface of Ag_3PO_4 [27]. Ag_2S nanoparticles show obvious adsorption capability (less than 20%) for MO because of the relatively high surface area. However, no decomposition of MO is observed in the presence of Ag_2S under visible light irradiation while pure Ag_3PO_4 can degrade 60% of MO after irradiation of 120 min. As compared, the Ag_2S-5%/Ag_3PO_4 sample exhibits much higher activity with respect to individual Ag_2S and Ag_3PO_4; the degradation of MO reaches nearly 100% after 120 min light irradiation. In addition, the physical mixture
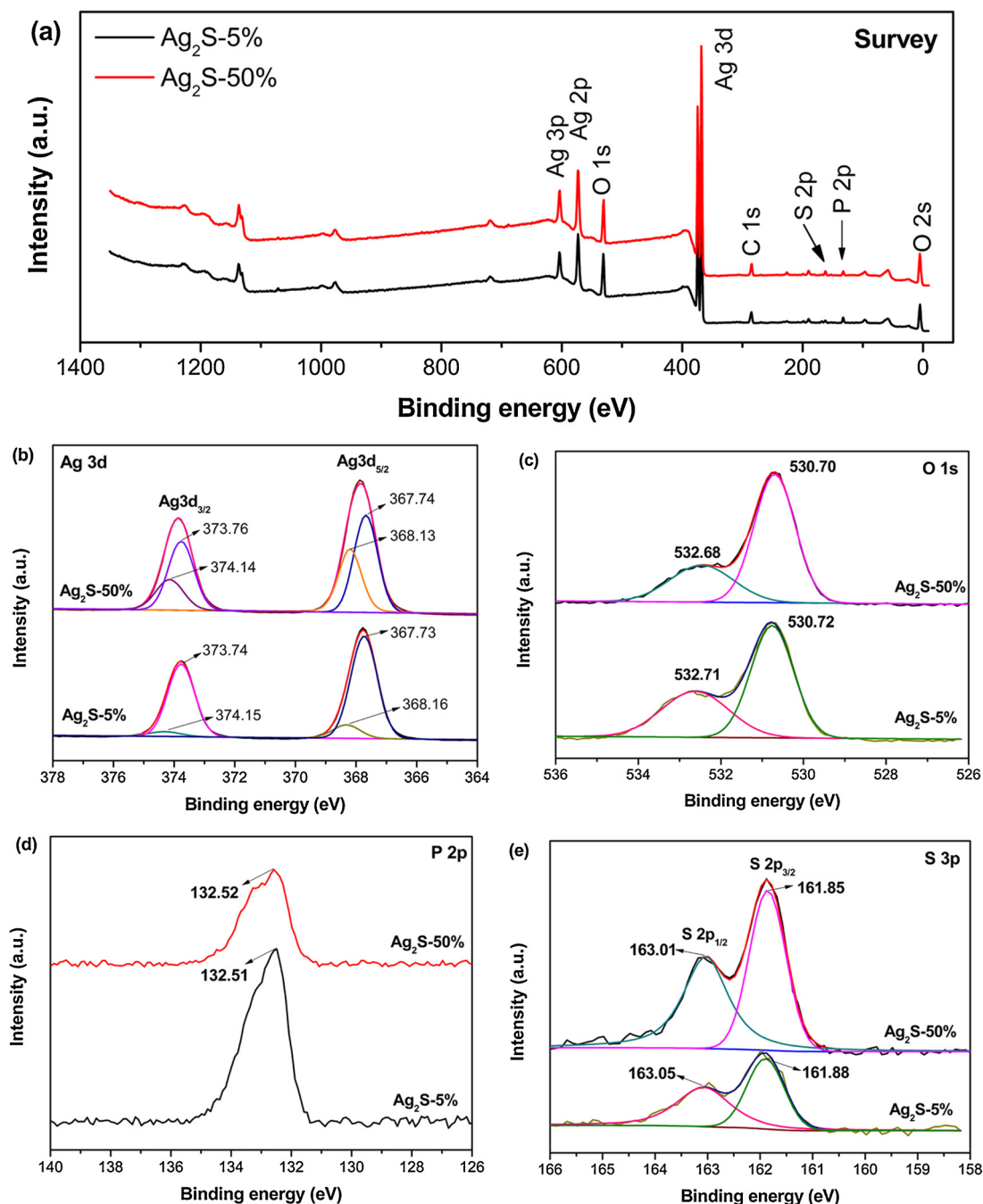
Fig. 4. XPS spectra of (a) survey (b) Ag 3d, (c) O 1s, (d) P 2p and (e) S 2p of the Ag_2S-5%/Ag_3PO_4 and Ag_2S-50%/Ag_3PO_4 composites.

of Ag_2S and Ag_3PO_4 at same Ag_2S content (5%) shows a lower photocatalytic activity compared to the ion-exchange synthesized Ag_2S-5%/Ag_3PO_4 composite. This may be attributed to the fact that the physically mixing of Ag_2S and Ag_3PO_4 results in poor contact between these two components, which hinders the interface charge transfer [47]. The photolysis of MO in the absence of photocatalyst is negligible within the test period as MO molecule is quite stable under visible light irradiation. No decomposition of MO is observed in dark even with catalyst, implying the importance of light irradiation.

The photocatalytic degradation kinetics towards the degradation of MO over various samples was investigated by fitting the experimental data to the Langmuir–Hinshelwood model. Since the concentration is low, the pseudo-first-order kinetic model might

be assumed as $-\ln(C/C_0) = kt$, where C_0 and C are the balanced and the final dye concentration, respectively, k is the pseudo-first order rate constant and t is light irradiation time. The results indicate that the reaction kinetics for all of the catalysts could be fitted to the pseudo-first-order kinetic model as presented in Fig. 6b. The visible-light-driven activity of Ag_2S/Ag_3PO_4 is highly dependent on the Ag_2S content. The Ag_2S/Ag_3PO_4 composites with low amount (1–5%) of Ag_2S show enhanced photocatalytic activity; however, excess Ag_2S (10–80%) result in the decrease of the photocatalytic activity (Fig. 6c). Among all composites, Ag_2S-5%/Ag_3PO_4 exhibits the most prominent photocatalytic activity and the maximum rate constant $(0.03388\,min^{-1})$, which is ∼4 and 176 times as high as that of Ag_3PO_4 $(0.00839\,min^{-1})$ and Ag_2S $(1.91883E-4)$, respectively. The Ag_2S-5%/Ag_3PO_4 composite also displays superior photocat-
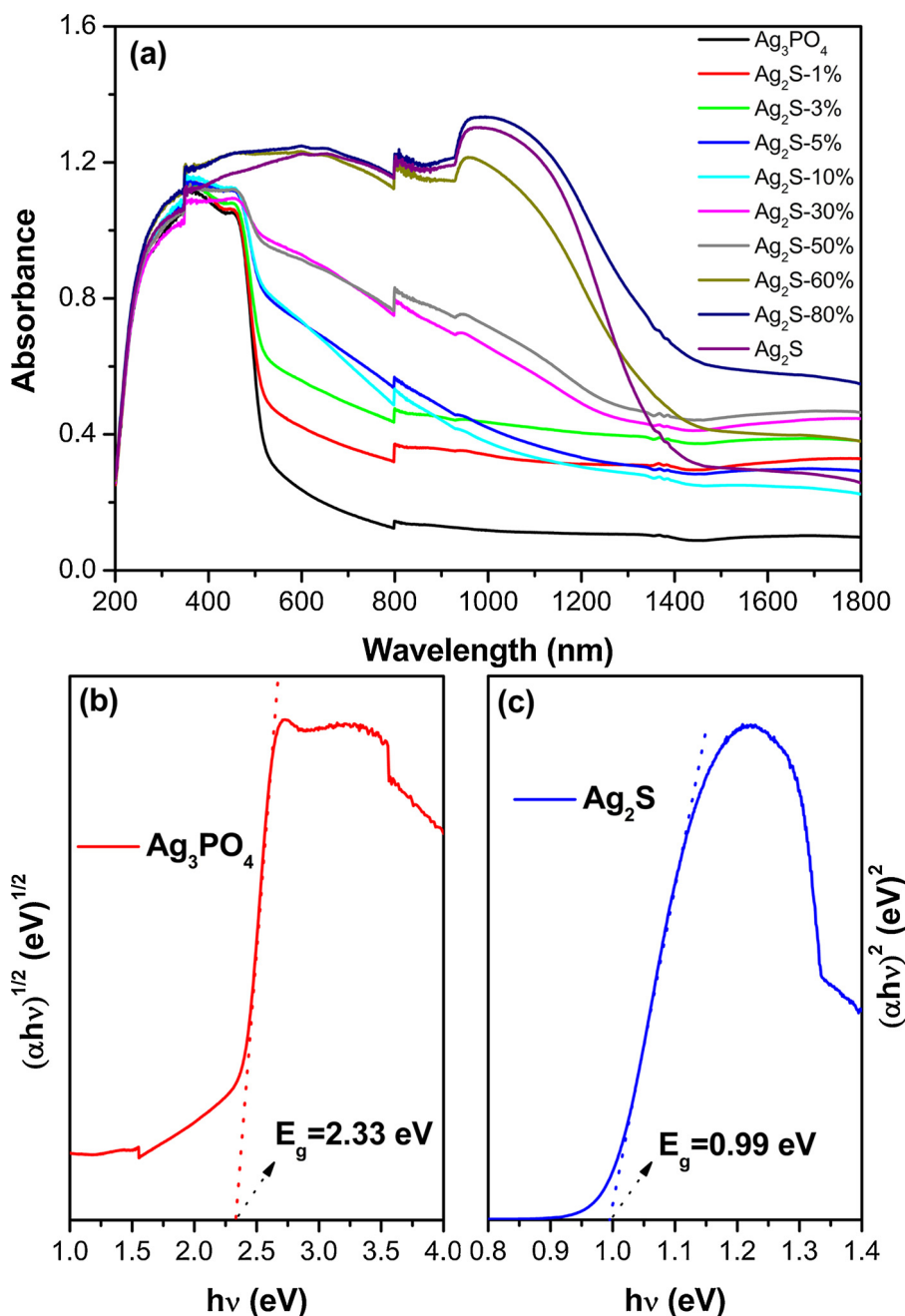
Fig. 5. (a) DRS spectra of Ag_3PO_4, Ag_2S, and Ag_2S/Ag_3PO_4 composites, (b and c) band gap energies of Ag_3PO_4 and Ag_2S.

alytic performance to Ag_3PO_4 towards the degradation of colorless chemical pollutants (*p*-chlorophenol and salicylic acid) under visible light irradiation (Fig. S5). As a result of quenching experiments shown in Fig. 6d, the photocatalytic degradation efficiency is largely suppressed after adding AO and BQ, indicating that h^+ and $O_2^{\bullet-}$ are the main active species over Ag_2S-5%/Ag_3PO_4 in the visible-light-driven photocatalytic process.

In addition to photocatalytic activity, stability is regarded as another important issue determining the practical application of photocatalysts, especially for Ag-based photocatalysts. Therefore, the cyclic degradation of MO under visible light over pure Ag_3PO_4 and Ag_2S-5%/Ag_3PO_4 composite was carried out. It can be seen that pure Ag_3PO_4 displayed an obvious deactivation during the repeated three experiments (Fig. S6). As compared, the Ag_2S-5%/Ag_3PO_4 composite exhibited excellent photocatalytic stability. As shown in Fig. 7a, the activity of Ag_2S-5%/Ag_3PO_4 reaches 99% after one

cycle (120 min) and remains at above 97% throughout the second and third cycles, indicating that Ag_2S-5%/Ag_3PO_4 composite acts as a stable photocatalyst. To check the phase of the used composite, XRD analysis is carried out on Ag_2S-5%/Ag_3PO_4 after three times recycle experiments. The XRD pattern in Fig. 7b shows that a new diffraction peak assigning to Ag appears at 38.06°, indicating the formation of metallic Ag during photocatalytic reaction. The microstructure and composition of Ag_2S-5%/Ag_3PO_4 after reaction are further investigated by TEM and EDX. From Fig. 7c, it can be clearly observed that many nanoparticles with size of about 40 nm are loaded on the Ag_2S/Ag_3PO_4 surface. These outside nanoparticles are only composed of Ag element (red region in Fig. 7c), while the inner samples consist of Ag, S, P and O elements (blue region in Fig. 7c), as evident by EDX in Fig. 7d and e. The Ag 3d XPS of used Ag_2S-5%/Ag_3PO_4 displays characteristic peaks attributing to metallic Ag and Ag^+ (Fig. S7). The calculated content of metallic Ag in the
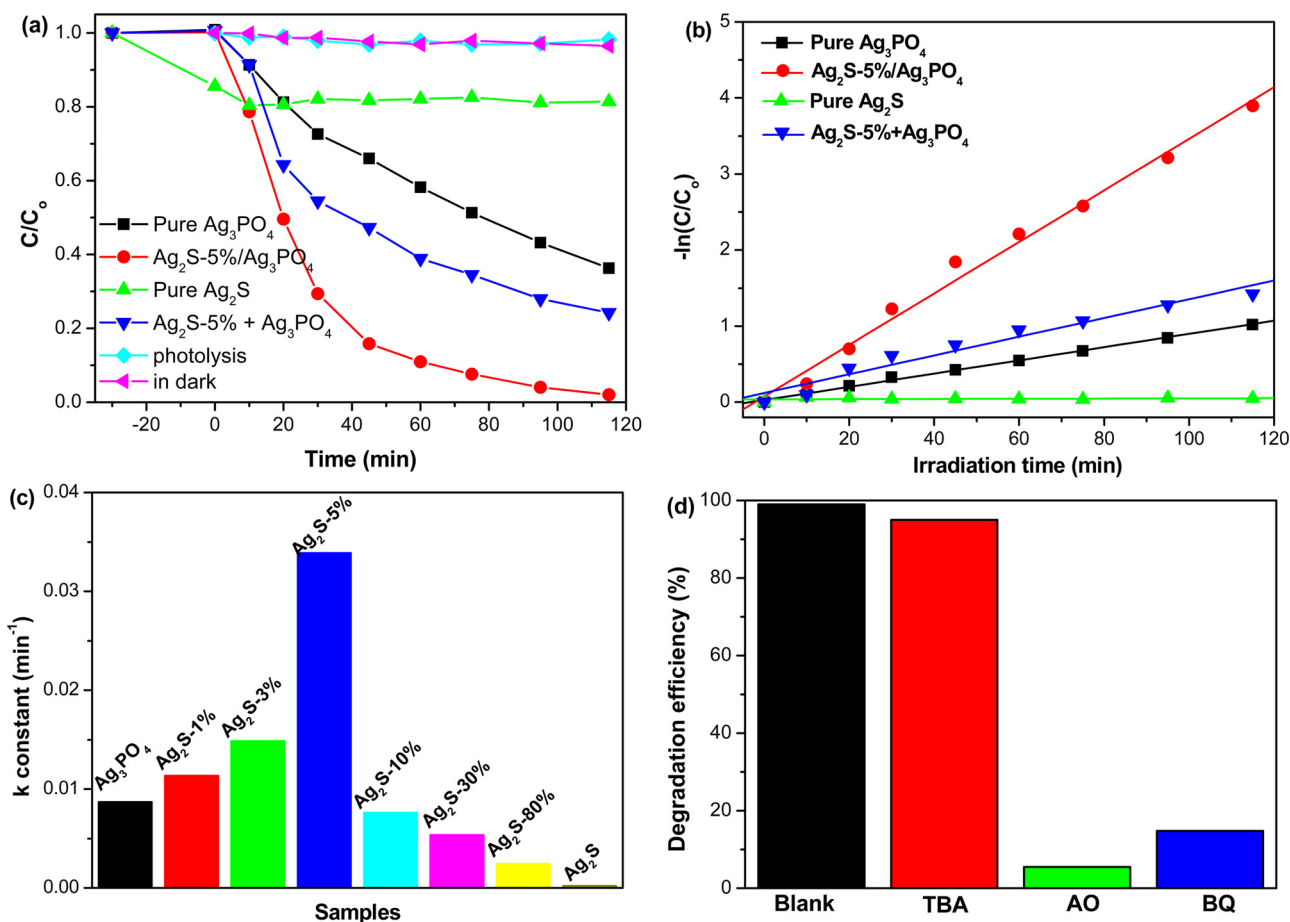
Fig. 6. (a) Photocatalytic degradation and (b) kinetic fit curves for the degradation of MO over various samples under visible light irradiation, (c) the corresponding rate constants, (d) effect of scavengers on the degradation efficiency of MO over Ag_2S-5%/Ag_3PO_4 under visible light irradiation.

used sample is about 13.3%, much higher than that in the fresh sample (7.5%). All these results show that some Ag^+ in Ag_2S/Ag_3PO_4 is reduced to Ag^0 during the photocatalytic experiments and a typical ternary photocatalyst $Ag_2S/Ag/Ag_3PO_4$ is *in-situ* formed (shown as the diagram in Fig. 7f).

On the basis of the above-mentioned results, a possible structural change and mechanism for MO degradation of Ag_2S/Ag_3PO_4 under visible light irradiation is proposed and shown in Scheme 1. Under visible light irradiation, both Ag_2S and Ag_3PO_4 are simultaneously excited and generate electron-hole pairs. The photoexcited electrons on more negative CB of Ag_2S (−0.025 eV) prefer to flow down to the CB of Ag_3PO_4 (0.25 eV) while the photoexcited holes would transfer from more positive VB of Ag_2S (0.965 eV) to the VB of Ag_3PO_4 (2.67 eV), resulting in an efficient charge separation process in Ag_2S/Ag_3PO_4. The electrons accumulated on the CB of Ag_3PO_4 are prone to combine with mobile interstitial silver ions from Ag_3PO_4 surfaces in the early photocatalytic process, leading to the formation of metallic Ag species and transforming the Ag_2S/Ag_3PO_4 into $Ag_2S/Ag/Ag_3PO_4$ ternary system eventually, like the reported $Ag_3PO_4/Ag/C_3N_4$, $Ag_3PO_4/Ag/TiO_2$, $Ag_3PO_4/Ag/AgI$ [25,37,48–50]. In these ternary systems, the *in-situ* formed Ag nanoparticles usually act as the charge transmission bridges, which can efficiently promote the separation of electron–hole pairs by a Z-scheme mechanism and ultimately enhance the photocatalytic performance. Our recent study on Ag_3PO_4/In_2S_3 also proved the formation of $Ag_3PO_4/Ag/In_2S_3$ Z-scheme system [39]. On the basis of the radical-trapping experiments and the similarity between Ag_2S/Ag_3PO_4 and Ag_3PO_4/In_2S_3, we believe that the Z-scheme mechanism might also work in the Ag_2S/Ag_3PO_4 composites under visible light irradiation.

Driven by the transmission bridge role of Ag nanoparticles, the electrons in CB of Ag_3PO_4 and the holes in VB of Ag_2S shift to metallic Ag simultaneously, which enhances the separation of electron–hole pairs and enables the holes and electrons to remain on Ag_3PO_4 and Ag_2S, respectively, accounting for the structural stability of the composites. The accumulated electrons in CB of Ag_2S can further reduce O_2 to initiate the yield of $O_2^{•−}$ reactive species which can decompose the MO pollutant. At the same time, the holes left on VB of Ag_3PO_4 with strong oxidation ability may oxidize $OH^−$ or H_2O to yield $•OH$. However, the present experimental results show that no $•OH$ species were generated in Ag_2S/Ag_3PO_4 system by the photoluminescence (PL) technology with terephthalic acid (TA) as a probe molecule (Fig. S8). Thiven by the transmission bridge role of Ag nanoparticles, the electrons in CB of Ag_3PO_4 and the holes in VB of Ag_2S shift to metallic Ag simultaneously, which enhances the separation of electron–hole pairs and enables the holes and electrons to remain on Ag_3PO_4 and Ag_2S, respectively, accounting for the structural stability of the composites. The accumulated electrons in CB of Ag_2S can further reduce O_2 to initiate the yield of $O_2^{•−}$ reactive species which can decompose the MO pollutant. At the same time, the holes left on VB of Ag_3PO_4 with strong oxidation ability may oxidize $OH^−$ or H_2O to yield $•OH$. However, the present experimental results show that no $•OH$ species were generated in Ag_2S/Ag_3PO_4 system by the photoluminescence (PL) technology with terephthalic acid (TA) as a probe molecule (Fig. S8). This declares that the holes reactive species would directly participate in the oxidation of MO.
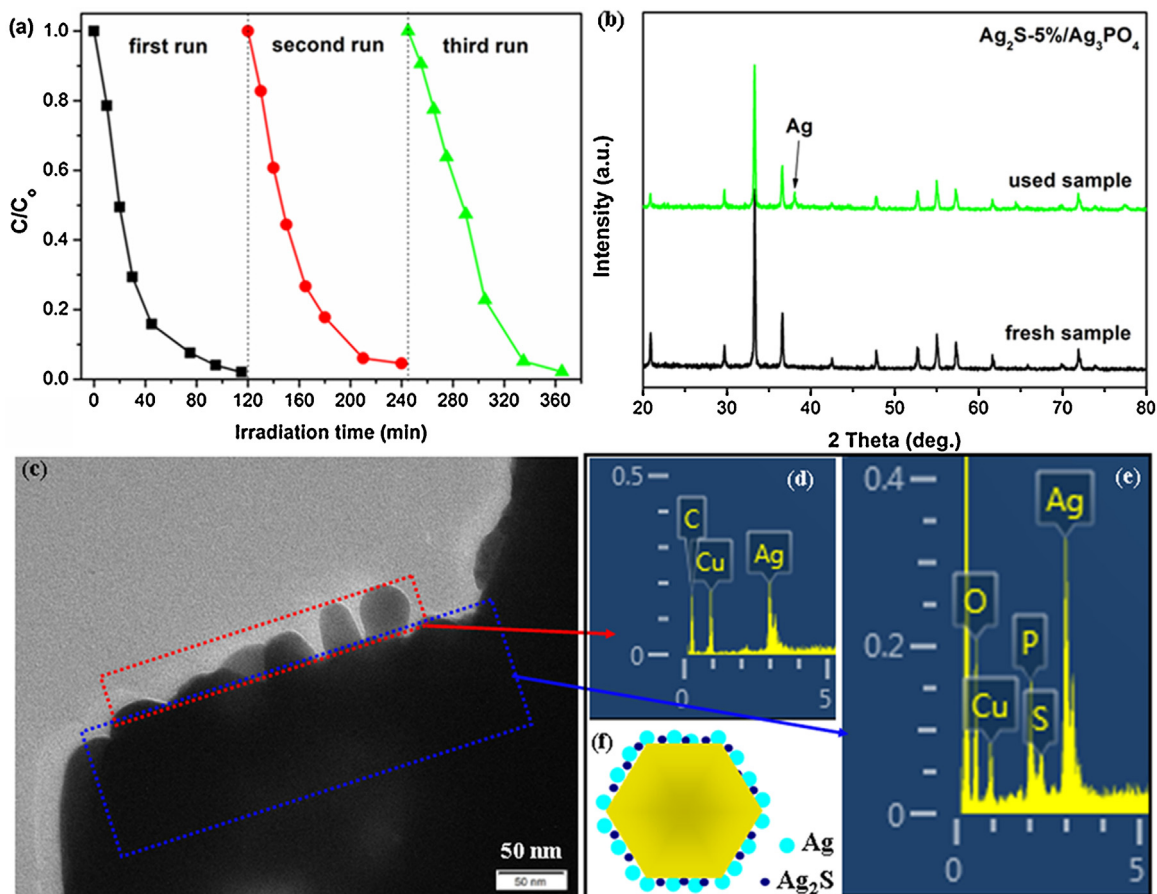
Fig. 7. (a) The cycling runs in photocatalytic degradation of MO over Ag$_2$S–5%/Ag$_3$PO$_4$ under visible light irradiation; (b) XRD patterns, (c) TEM and (d and e) EDX patterns of Ag$_2$S–5%/Ag$_3$PO$_4$ after photocatalytic reaction, (f) the diagram for the Ag$_2$S/Ag/Ag$_3$PO$_4$ system. (For interpretation of the references to color in this figure legend, the reader is referred to the web version of this article.)
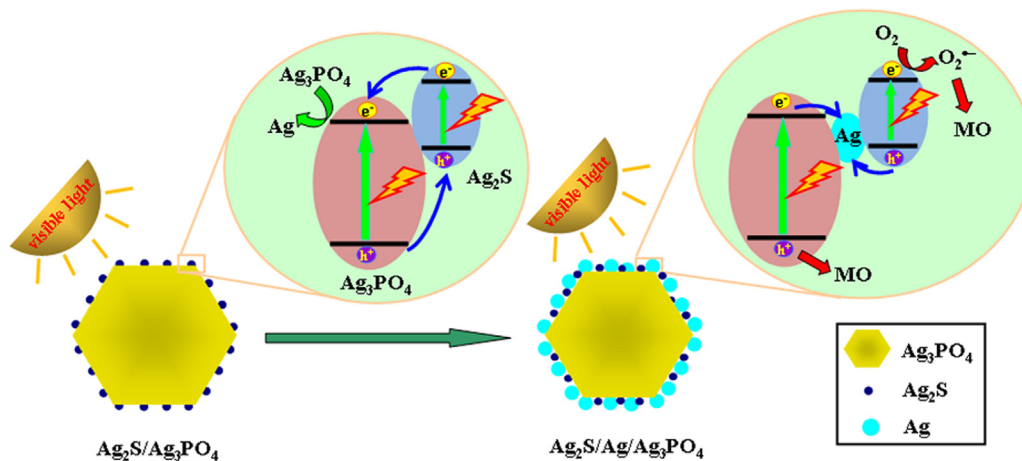
Scheme 1. The proposed structural change and mechanism for MO degradation of Ag$_2$S/Ag$_3$PO$_4$ under visible light irradiation.

3.4.2. NIR-light-driven photocatalytic property

In this work, except for the visible light photocatalytic property, we find Ag$_2$S/Ag$_3$PO$_4$ composites also possess excellent NIR-light-driven photocatalytic activity for MO. As shown from Fig. 8a, the Ag$_2$S–50%/Ag$_3$PO$_4$ composite displays superior activity to pure Ag$_2$S and Ag$_3$PO$_4$, as well as the physically mixed Ag$_2$S/Ag$_3$PO$_4$. The photocatalytic reaction for the catalysts is all fitted to the pseudo-first-order kinetic model (Fig. 8b). Similarly, the NIR-light-driven

activity of Ag$_2$S/Ag$_3$PO$_4$ is also closely related to the Ag$_2$S contents. As compared to pure Ag$_2$S and Ag$_3$PO$_4$, excellent photocatalytic activities are observed on the Ag$_2$S/Ag$_3$PO$_4$ composites with Ag$_2$S loading of 10–50% (Fig. 8c). Among these composites, the Ag$_2$S–50%/Ag$_3$PO$_4$ sample exhibits the highest activity and rate constant (0.00143 min^{-1}). Fig. 8d displays the trapping experiment of active species for MO degradation over Ag$_2$S–50%/Ag$_3$PO$_4$ under NIR light
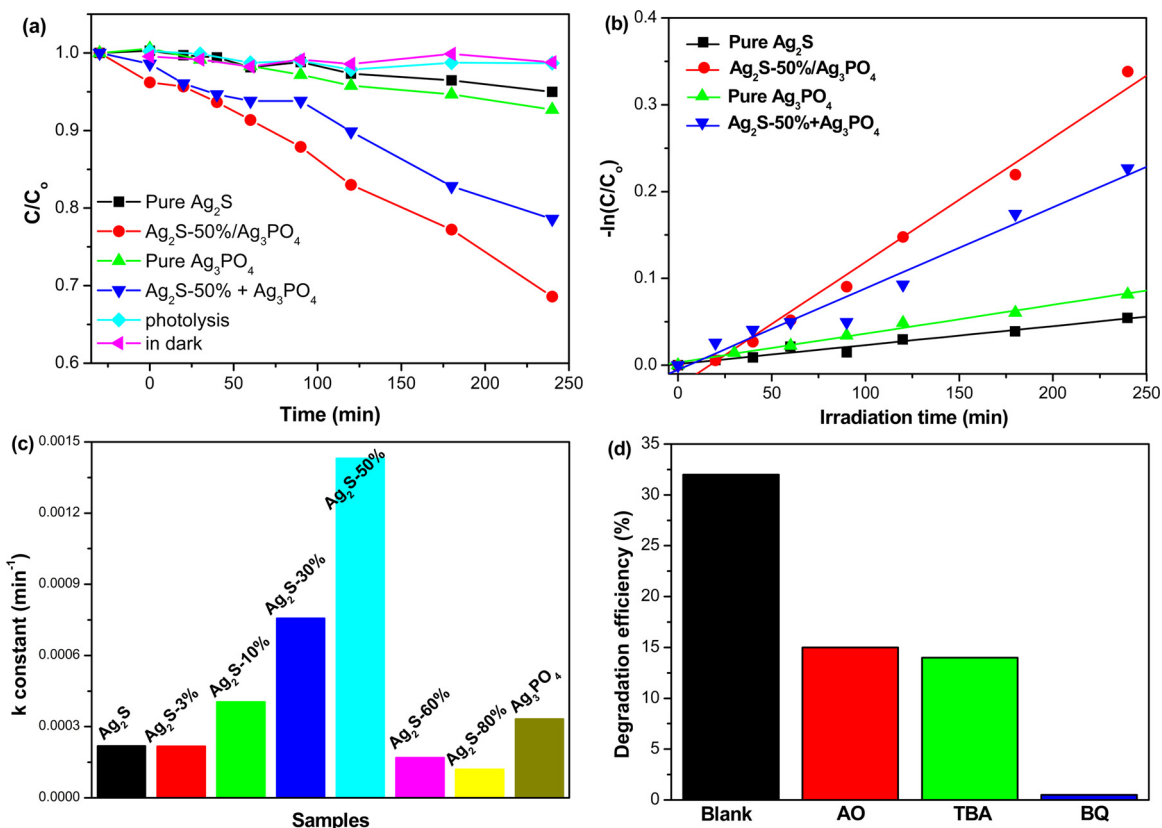
Fig. 8. (a) Photocatalytic degradation and (b) kinetic fit curves for the degradation of MO over various samples under NIR light irradiation, (c) the corresponding rate constants, (d) effect of scavengers on the degradation efficiency of MO over Ag_2S-50%/Ag_3PO_4 under NIR light irradiation.

irradiation. It can be concluded that the main active species are $O_2{}^{\bullet-}$, h^+ and $\bullet OH$.

The photocatalytic stability of Ag_2S-50%/Ag_3PO_4 composite is also investigated for the cyclic degradation of MO under NIR light irradiation. As shown in Fig. 9a, after three continuous cycles of photodegradation, the Ag_2S-50%/Ag_3PO_4 catalyst does not exhibit obvious loss of activity, demonstrating its good recyclability. The XRD patterns (Fig. 9b) reveal that the catalyst collected after the photocatalytic experiments keeps the main Ag_3PO_4 phase and has an additional small peak assigning to metallic Ag. The used Ag_2S-50%/Ag_3PO_4 composite inherits the original core/shell structure (Fig. 9c). From the enlarged TEM image in Fig. 9d, we can see that some tiny nanoparticles with average size of 15 nm are dispersed on the surfaces of large Ag_2S particles. The EDX spectrum (Fig. 9e) indicates that these tiny nanoparticles are mainly composed of Ag element. The increased content (73.1%) of metallic Ag in the used Ag_2S-50%/Ag_3PO_4 composite calculated from the Ag 3d XPS spectrum also supports the new formation of metallic Ag nanoparticles (Fig. S9). Considering the full cover of Ag_3PO_4 by Ag_2S, it is inferred that the newly formed tiny nanoparticles are metallic Ag, which originate from the *in-situ* photoreduction of Ag_2S. Thus, a new $Ag/Ag_2S/Ag_3PO_4$ system is formed during the photocatalytic process (Fig. 9f).

A possible structural change and photocatalytic mechanism of Ag_2S/Ag_3PO_4 under NIR light irradiation is also proposed in Scheme 2. Ag_2S with a narrow band gap energy (0.99 eV) can be easily excited by NIR light ($\lambda > 760$ nm) and induce the generation of electrons and holes. In the case of Ag_3PO_4, it cannot be excited by NIR irradiation with energy less than 2.75 eV. The matched band structure between Ag_2S and Ag_3PO_4 favored the electrons transfer from Ag_2S to Ag_3PO_4. However, the full cover of Ag_2S nanoparticles on Ag_3PO_4 surfaces effectively protects it from dissociation into

interstitial silver ions, inhibiting the reduction of Ag_3PO_4 to metallic Ag by photogenerated electrons. Instead, the gathered electrons on Ag_3PO_4 can react with adsorbed O_2 to yield H_2O_2 and then $\bullet OH$ [31]. The generation of H_2O_2 over Ag_2S-50%/Ag_3PO_4 under NIR light irradiation was determined by the DPD method [51]. The results show that the photogeneration of H_2O_2 occurred throughout the process and its concentration increased rapidly within the first 30 min and reached a plateau value after approximately 150 min (Fig. S10). Alternatively, the photogenerated electrons over Ag_2S could also react with itself to form Ag^0 (Fig. 9d) [42]. The formed Ag^0 species will function as electrons traps to capture photogenerated electrons from CB of Ag_2S and react with adsorbed O_2 to generate $O_2{}^{\bullet-}$. These generated $O_2{}^{\bullet-}$ and $\bullet OH$ radicals, together with holes left at the VB of Ag_2S, act as the main active species and finally degrade dye molecules (Fig. 8d).

It is concluded that the improved photocatalytic activity (both visible and NIR light) of Ag_2S/Ag_3PO_4 composites is highly dependent on the well-defined core/shell structure. The well interfacial contact in composite photocatalysts greatly promotes the charge carries transfer and separation and thus the photocatalytic performance. To justify this assumption, we use PL spectroscopy to survey the extent of charge separation of the pure Ag_3PO_4 and Ag_2S/Ag_3PO_4 composites. Steady-state PL spectra were first investigated and the results are shown in Fig. 10a. Pure Ag_3PO_4 show a broad emission band ranging from 480 to 600 nm. The strong emission peak at around 550 nm, which has a photon energy approximately equal to the band gap of Ag_3PO_4, is considered to originate from the recombination of photogenerated electrons and holes [47,52]. It can be observed that the PL spectra of both Ag_2S/Ag_3PO_4 composites are similar to that of pure Ag_3PO_4, but the overall emission intensity is significantly weakened, which implies that the recombination of photogenerated electrons and holes is
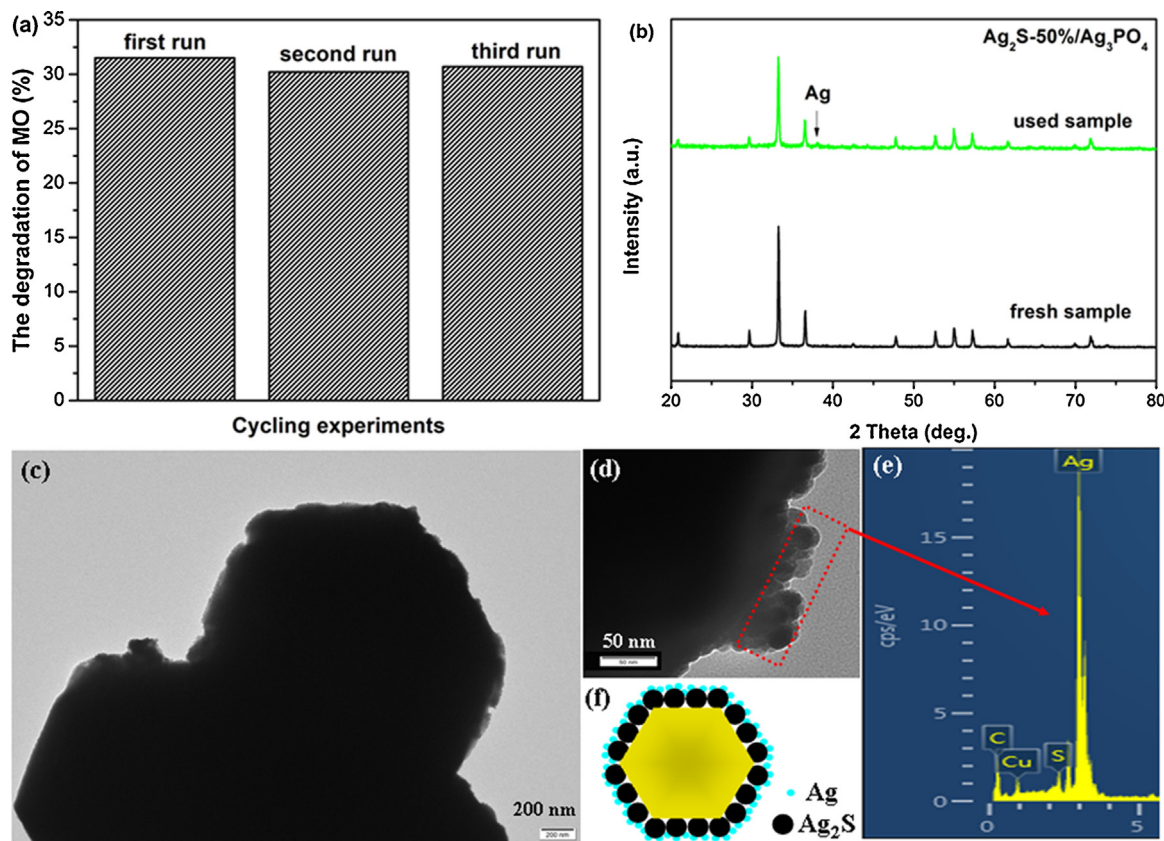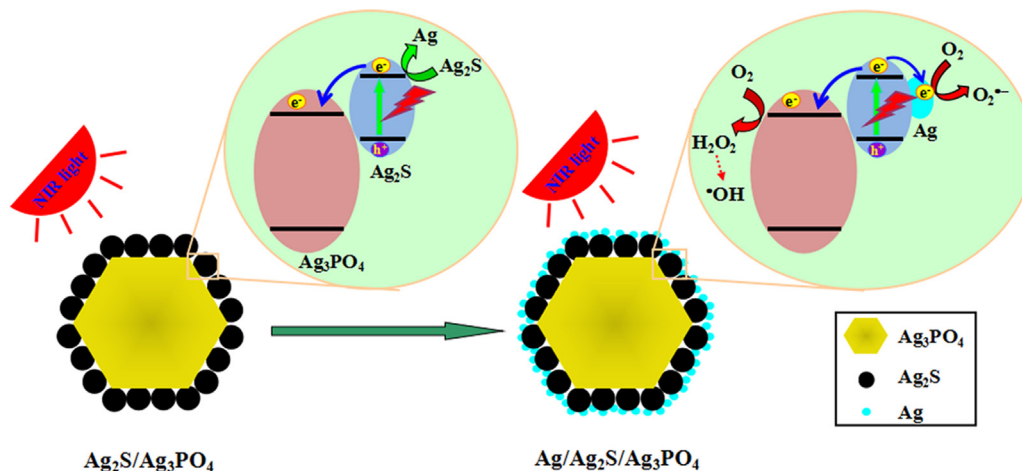
Fig. 9. The cycling runs in photocatalytic degradation of MO over Ag_2S-50%/Ag_3PO_4 under NIR light irradiation; (b) XRD patterns, (c and d) TEM and (e) EDX patterns of Ag_2S-50%/Ag_3PO_4 after photocatalytic reaction, (f) the diagram for the $Ag/Ag_2S/Ag_3PO_4$ system.

Scheme 2. The proposed structural change and mechanism for MO degradation of Ag_2S/Ag_3PO_4 under NIR light irradiation.

effectively prevented in the Ag_2S/Ag_3PO_4 composites [53]. As compared to the physical mixture of Ag_2S and Ag_3PO_4, the Ag_2S/Ag_3PO_4 composites also display decreased PL intensity, further suggesting the important feature of core/shell structures in enhancing charge carries separation. Time-resolved PL spectra were further performed. As shown in Fig. 10b, the average life time for pure Ag_3PO_4 was 3.17 ns while it increased to 3.62 ns and 3.24 ns for Ag_2S-5%/Ag_3PO_4 and Ag_2S-50%/Ag_3PO_4, respectively. A longer lifetime of the excited state means the photogenerated charge carrier can go further before it decays back to the ground state, leading to more efficient electron–hole separation. Fig. 10c shows the EIS spectra obtained at the interface between the electrolyte and

photocatalysts. The diameters of the arc radii of Ag_2S-5%/Ag_3PO_4 and Ag_2S-50%/Ag_3PO_4 are clearly much smaller than that of pure Ag_3PO_4, also indicating a higher efficiency of charge transfer on the surface of the Ag_2S/Ag_3PO_4 composites.

On the other hand, the Ag_2S content is also crucial to influence the photocatalytic activity of Ag_2S/Ag_3PO_4 composites. Under visible light irradiation, since both Ag_2S and Ag_3PO_4 need to be excited, a partial cover of Ag_2S over Ag_3PO_4 surface is necessary and thus a low amount of Ag_2S benefits the light absorbance and charge carries transfer. Along with the *in-situ* formation of metallic Ag at Ag_3PO_4 surfaces, a stable and well-defined $Ag_2S/Ag/Ag_3PO_4$ Z-scheme system ensures the excellent photocatalytic performance towards
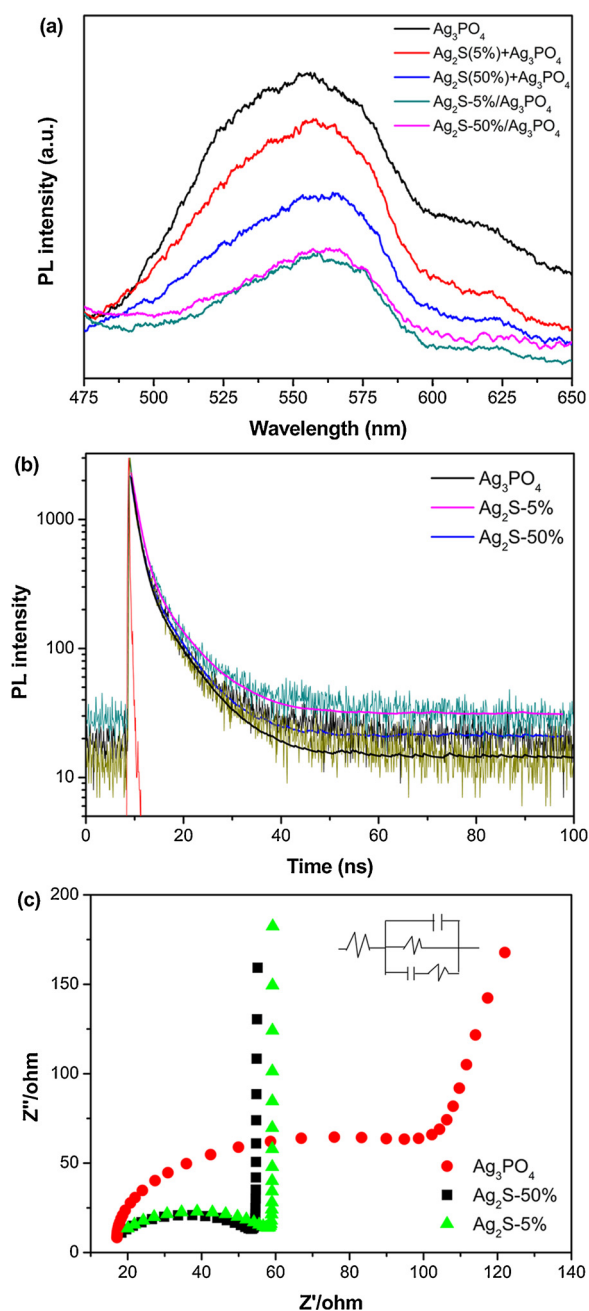
Fig. 10. (a) Steady-state PL (λ_{ex} = 320 nm), (b) time-resolved PL spectra, and (c) EIS Nyquist plots for pure Ag$_3$PO$_4$ and Ag$_2$S/Ag$_3$PO$_4$ composites.

MO degradation. In the case of NIR light irradiation, the activity enhancement of Ag$_2$S/Ag$_3$PO$_4$ composites mainly arises from the sensitization effect of Ag$_2$S. Thus, the more Ag$_2$S load on the Ag$_3$PO$_4$ surfaces, the more photons generate and the higher photocatalytic activity is. However, with excess Ag$_2$S in the Ag$_2$S/Ag$_3$PO$_4$ composites, the well-contact interface between Ag$_2$S and Ag$_3$PO$_4$ is greatly destroyed. In this case, the electrons generated in Ag$_2$S are unfavorable to transfer to Ag$_3$PO$_4$ but combine easily with holes at Ag$_2$S itself, resulting in the decreased photocatalytic activity therefore.

4. Conclusions

Highly robust Ag$_2$S/Ag$_3$PO$_4$ core/shell composites with different Ag$_2$S contents have been prepared by the simple anion-exchange method. The photocatalytic activity and stability of Ag$_3$PO$_4$ towards

MO degradation under both visible and NIR light are greatly improved by the introduction of Ag$_2$S. The enhanced activity of Ag$_2$S/Ag$_3$PO$_4$ composites is due to the effective separation and fast transfer of photogenerated charge carriers. The photocatalytic mechanism study highlights that the *in-situ* formed metallic Ag, can respectively act as charge transmission bridges and electron traps under visible and NIR light irradiation, and further help to construct the stable Ag$_2$S/Ag/Ag$_3$PO$_4$ and Ag/Ag$_2$S/Ag$_3$PO$_4$ systems. This research shows the possibility of utilizing Ag$_2$S as photosensitizer or appropriate narrow-band-gap semiconductor to achieve highly efficient composite photocatalysts working under visible and NIR light irradiation.

Appendix A. Supplementary data

Supplementary data associated with this article can be found, in the online version, at http://dx.doi.org/10.1016/j.apcatb.2017.03.022.

References

[1] A. Fujishima, K. Honda, Nature 238 (1972) 37–38.
[2] Y.H. Sang, H. Liu, A. Umar, ChemCatChem 7 (2015) 559–573.
[3] B. Cao, G.S. Li, H.X. Li, Appl. Catal., B: Environ. 194 (2016) 42–49.
[4] R. Asahi, T. Morikawa, T. Irie, T. Ohwaki, Chem. Rev. 114 (2014) 9824–9852.
[5] X.J. Bai, L. Wang, Y.F. Zhu, ACS Catal. 2 (2012) 2769–2778.
[6] W.P. Qin, D.S. Zhang, D. Zhao, L.L. Wang, K.Z. Zheng, Chem. Commun. 46 (2010) 2304–2306.
[7] Z.G. Zou, J.H. Ye, K. Sayama, H. Arakawa, Nature 414 (2001) 625–627.
[8] Z.B. Lei, W.S. You, M.Y. Liu, G.H. Zhou, T. Takata, M. Hara, K. Domen, C. Li, Chem. Commun. 9 (2003) 2142–2143.
[9] X.C. Wang, K. Maeda, A. Thomas, K. Tazuhiro, G. Xin, J.M. Carlsson, K. Domen, M. Antonietti, Nat. Mater. 8 (2009) 76–80.
[10] P. Wang, B.B. Huang, X.Y. Qin, X.Y. Zhang, Y. Dai, J.Y. Wei, M.H. Whangbo, Angew. Chem. Int. Ed. 47 (2008) 7931–7933.
[11] G. Wang, B.B. Huang, X.C. Ma, Z.Y. Wang, X.Y. Qin, X.Y. Zhang, Y. Dai, M.H. Whangbo, Angew. Chem. Int. Ed. 52 (2013) 4810–4813.
[12] Z.G. Yi, J.H. Ye, N. Kikugawa, T. Kako, S.X. Quang, H.S. Williams, H. Yang, J.Y. Cao, W.J. Luo, Z.S. Li, Y. Liu, R.L. Withers, Nat. Mater. 9 (2010) 559–564.
[13] Y.P. Bi, S.X. Ouyang, N. Umezawa, J.Y. Cao, J.H. Ye, J. Am. Chem. Soc. 133 (2011) 6490–6492.
[14] Y.P. Bi, H.Y. Hu, S.X. Ouyang, Z.B. Jiao, G.X. Lu, J.H. Ye, J. Mater. Chem. 22 (2012) 14847–14850.
[15] H.Y. Hu, Z.B. Jiao, T. Wang, J.H. Ye, G.X. Lu, Y.P. Bi, J. Mater. Chem. A 1 (2013) 10612–10616.
[16] N. Tian, H.W. Huang, C.Y. Liu, F. Dong, T.R. Zhang, X. Du, S.X. Yu, Y.H. Zhang, J. Mater. Chem. A 3 (2015) 17120–17129.
[17] H.W. Huang, X. Han, X.W. Li, S.C. Wang, P.K. Chu, Y.H. Zhang, ACS Appl. Mater. Interfaces 7 (2015) 482–492.
[18] H.W. Huang, K. Xiao, Y. He, T.R. Zhang, F. Dong, X. Du, Y.H. Zhang, Appl. Catal., B: Environ. 199 (2016) 75–86.
[19] H.W. Huang, K. Xiao, T.R. Zhang, F. Dong, Y.H. Zhang, Appl. Catal., B: Environ. 203 (2017) 879–888.
[20] W.F. Yao, B. Zhang, C.P. Huang, C. Ma, X.L. Song, Q.J. Xu, J. Mater. Chem. 22 (2012) 4050–4055.
[21] J.J. Guo, S.X. Ouyang, H. Zhou, T. Kako, J.H. Ye, J. Phys. Chem. C 117 (2013) 17716–17724.
[22] C.J. Li, P. Zhang, R. Lv, J.W. Lu, T. Wang, S.P. Wang, H.F. Wang, J.L. Gong, Small 9 (2013) 3951–3956.
[23] Y.Q. Wang, X.F. Cheng, X.T. Meng, H.W. Feng, S.G. Yang, C. Sun, J. Alloy. Compd. 632 (2015) 445–449.
[24] L.L. Zhang, H.C. Zhang, H. Huang, Y. Liu, Z.H. Kang, New J. Chem. 36 (2012) 1541–1544.
[25] Y.M. He, L.H. Zhang, B.T. Teng, M.H. Fan, Environ. Sci. Technol. 49 (2014) 649–656.
[26] G.D. Chen, M. Sun, Q. Wei, Y.F. Zhang, B.C. Zhu, B. Du, J. Hazard. Mater. 244 (2013) 86–93.

[27] T.J. Yan, W.F. Guan, W.J. Li, J.M. You, RSC Adv. 4 (2014) 37095–37099.
[28] H.F. Cheng, B.B. Huang, P. Wang, Z.Y. Wang, Z.Z. Lou, J.P. Wang, X.Y. Qin, X.Y. Zhang, Y. Dai, Chem. Commun. 47 (2011) 7054–7056.
[29] N. Zhang, S.Q. Liu, Y.J. Xu, Nanoscale 4 (2012) 2227–2238.
[30] H.C. Yu, Q.S. Dong, Z.B. Jiao, T. Wang, J.T. Ma, G.X. Lu, Y.P. Bi, J. Mater. Chem. A 2 (2014) 1668–1671.
[31] Y.P. Bi, S.X. Ouyang, J.Y. Cao, J.H. Ye, Phys. Chem. Chem. Phys. 13 (2011) 10071–10075.
[32] L. Liu, Y.H. Qi, J.Y. Lu, S.L. Lin, W.J. An, Y.H. Liang, W.Q. Cui, Appl. Catal., B: Environ. 193 (2016) 133–141.
[33] G.X. Zhu, Z. Xu, J. Am. Chem. Soc. 133 (2010) 148–157.
[34] W.L. Yang, L. Zhang, Y. Hu, Y.J. Zhong, H.B. Wu, X.W. Lou, Angew. Chem. Int. Ed. 51 (2012) 11501–11504.
[35] S. Khanchandani, P.K. Srivastava, S. Kumar, S. Ghosh, A.K. Ganguli, Inorg. Chem. 53 (2014) 8902–8912.
[36] W. Jiang, Z.M. Wu, X.N. Yue, S.J. Yuan, H.F. Lu, B. Liang, RSC Adv. 5 (2015) 24064–24071.
[37] Y.R. Li, L.L. Li, Y.Q. Gong, S. Bai, H.X. Ju, C.M. Wang, Q. Xu, J.F. Zhu, J. Jiang, Y.J. Xiong, Nano Res. 8 (2015) 3621–3629.
[38] J.T. Tang, W. Gong, T.J. Cai, T. Xie, C. Deng, Z.S. Peng, Q. Deng, RSC Adv. 3 (2013) 2543–2547.
[39] P.Y. Ma, H.J. Yu, Y. Yu, W.M. Wang, H. Wang, J.Y. Zhang, Z.Y. Fu, Phys. Chem. Chem. Phys. 18 (2016) 3638–3643.
[40] T.J. Yan, J. Tian, W.F. Guan, Z. Qiao, W.J. Li, J.M. You, B.B. Huang, Appl. Catal., B: Environ. 202 (2017) 84–94.
[41] H.L. Zhang, B. Wei, L. Zhu, J.H. Yu, W.J. Sun, L.L. Xu, Appl. Surf. Sci. 270 (2013) 133–138.
[42] M.L. Pang, J.Y. Hu, H.C. Zeng, J. Am. Chem. Soc. 132 (2010) 10771–10785.
[43] D.L. Jiang, L.L. Chen, J.M. Xie, M. Chen, Dalton Trans. 43 (2014) 4878–4885.
[44] T. Zhu, C. Zhang, G.W. Ho, J. Phys. Chem. C 119 (2015) 1667–1675.
[45] W.G. Wang, B. Cheng, J.G. Yu, G. Liu, W.H. Fan, Chem. Asian J 7 (2012) 1902–1908.
[46] D.S. Wang, C.H. Hao, W. Zheng, Q. Peng, T.H. Wang, Z.M. Liao, D.P. Yu, Y.D. Li, Adv. Mater. 20 (2008) 2628–2632.
[47] Q.H. Liang, Y. Shi, W.J. Ma, Z. Li, X.M. Yang, Phys. Chem. Chem. Phys. 14 (2012) 15657–15665.
[48] X.F. Yang, Z.P. Chen, J.S. Xu, H. Tang, K.M. Chen, Y. Jiang, ACS Appl. Mater. Interfaces 7 (2015) 15285–15293.
[49] W. Teng, X.Y. Li, Q.D. Zhao, G.H. Chen, J. Mater. Chem. A 1 (2013) 9060–9068.
[50] Z.H. Chen, W.L. Wang, Z.G. Zhang, X.M. Fang, J. Phys. Chem. C 117 (2013) 19346–19352.
[51] R.R. Wang, K.C. Pan, D.D. Han, J.J. Jiang, C.X. Xiang, Z.Q. Huang, L. Zhang, X. Xiang, ChemSusChem 9 (2016) 1–11.
[52] L. Wang, Y.Y. Chai, J. Ren, J. Ding, Q.Q. Liu, W.L. Dai, Dalton Trans. 44 (2015) 14625–14634.
[53] X.F. Chen, X.C. Wang, Y.D. Hou, J.H. Huang, L. Wu, X.Z. Fu, J. Catal. 255 (2008) 59–67.